2020 IEEE International Conference on Robotics and Automation (ICRA)
31 May - 31 August, 2020. Paris, France

Highly sensitive bio-inspired sensor for fine surface exploration and characterization

Pedro Ribeiro[1,2,4], Susana Cardoso[1,2], Alexandre Bernardino[3] and Lorenzo Jamone[4]

***Abstract*— Texture sensing is one of the types of information sensed by humans through touch, and is thus of interest to robotics that this type of information can be acquired and processed. In this work we present a texture topography sensor based on a ciliary structure, a biological structure found in many organisms. The device consists of up to 9 elastic cilia with permanent magnetization assembled on top of a highly sensitive tunneling magnetoresistance (TMR) sensor, within a compact footprint of 6x6 mm^2. When these cilia brush against some textured surface, their movement and vibrations give rise to a signal that can be correlated to the characteristics of the texture being measured. We also present an electronic signal acquisition board, used in this work. Various configurations of cilia sizes are tested, with the most precise being capable of differentiating different types of sandpaper from 9.2 μm to 213 μm average surface roughness with a 7 μm resolution. As a topography scanner the sensor was able to scan a 20 μm high step in a flat surface.**

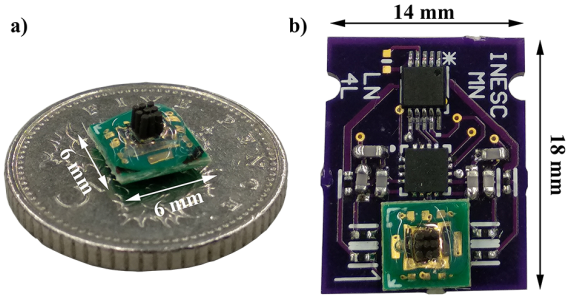

Fig. 1. a) Sensing element, mounted on a 6x6 mm^2 PCB with the connector on the backside. The cilia in this element are arranged in a 3x3 configuration with 1.6 mm height and 360 μm diameter. b) Texture topography sensor assembled with the data acquisition and conversion board.

I. INTRODUCTION

Information about the manipulable world through tactile perception would provide robots with a great amount of information that is usually not available through vision (since objects being manipulated are usually occluded by a manipulating tool, such as a robotic hand [1]), allowing these to operate in unstructured and unpredictable environments with a greater amount of control and ultimately enabling safe human-robot cooperation [2].

Furthermore, it is of interest that these sensors use either a high-resolution transducer (with at least 1 sensed point per mm^2) or be made within compact footprints to enable high spatial resolutions [3]. In what concerns texture detection, two types of transduction technologies have been commonly used in the past. Optical based technologies, where the device uses a camera [4] or a photodetector [5], in conjunction with some light emitting element (such as LEDs or fibre optics) to measure and analyze the texture over a localized area, usually with great spatial resolution; or acoustic based transducers, employing an array of microphones and applying a vibration, and correlating the sound amplitude measured by the microfones with the type of texture that is actuating the sensor [6].

Although these devices are capable of resolving complex ordered and unordered textures, these tend to be bulky, which brings integration challenges with existing robotic platforms as well as excessive power consumption. To overcome this, other transducing tecnologies have been emerging for texture sensing, with piezoelectric transducers being the most promising. Surface roughness measurements down to 400 nm [7] and topographical scanning capable of resolving features with 25 μm thickness [8] have been reported.

Another organelle capable of detecting forces, textures and flows is the cilium, a structure that consists of a passive hair-like structure attached to a dendrite, an active organnelle that sends electrical impluses when the cilium is actuated. This structure is present in many types of different biological organisms, from humans to unicelular beings [9].

The ciliary structure was first identified and developed as a sensor for fluid flows in microfluidic systems, mostly as a rigid cilia with piezoelectric [10] or capacitive detection principles [11]. To overcome the brittleness of rigid cilia (which made these sensors unsuitable for force sensing, as these could break upon contact), the usage of an elastomeric compound with embedded magnetic material was initially proposed in [12], using an evaporation process. Despite enabling force quantification, this strategy was not compatible with device engineering, as the pillars were grown randomly over the sensor surface.

The molding of such permanently magnetized elastic composites appeared due to the necessitity of fabricating more robust cilia for flow sensing systems [13], but was soon after tested as a force sensing system, initially by using giant magnetoimpedance sensors [14] and later by using more compact, sensitive and energetically efficient giant magnetoresistive sensors [15].

Although force testing has been validated for cilia sensors across the cited works, texture quantification and classification with ciliary sensors has not been profoundly studied,

[1]INESC - Microsystems and Nanotechnologies, Lisbon, Portugal
[2]Department of Physics, Instituto Superior Técnico, University of Lisbon, Portugal
[3]Institute for Systems and Robotics, Lisbon, Portugal
[4]ARQ, School of Electronic Engineering and Computer Science, Queen Mary University of London, London, United Kingdom

with a braille reading sensor capable of binary topography sensing [16] and determination of sandpaper surface roughness [17] being reported in literature.

In this work, we present a ciliary texture topography sensor based on flexible magnetic polydimethylsiloxane (PDMS) pillars, with the following improvements over previously reported devices (Fig. 1):

- **Magnetic cilia**: Optimized process, with more magnetic particles and a thermal treatment, yielding a much higher magnetic signal and thus better signal-to-noise ratios.
- **TMR sensor**: A tunnel magnetoresistance based sensor (TMR) technology is used, more sensitive and power efficient when compared with other magnetoresistive technologies used in devices previously reported in literature. Furthermore, an improved 2D Wheatstone bridge architecture technology is used, resulting in easier integration, signal acquisition and reduced noise.
- **Analog front-end**: An analog front-end was developed, allowing analog offset correction, low-pass filtering and analog-to-digital conversion in a small 14x18 mm^2 footprint supporting I^2C output, further facilitating the integration of this device with robotic platforms.

Given the achieved developments, the device was tested as a surface roughness measurement device for micrometric unpatterned textures (e.g. sandpaper) and as a topographic scanner in patterned structures, capable of detecting sub-100 μm thick features.

II. Sensor fabrication and assembly

The developed sensing device was designed with the goal of imitating a ciliary structure, which is composed by a passive organellum (the cilium itself) attached to an active organellum (dendrite) at its root that converts any movement of the cilium into electrical impulses.

For our device, the passive organellum is an array of PDMS pillars with embedded NdFeB permanently magnetized particles, and a TMR based sensor at its base measuring the incident magnetic field from these magnetized pillars. Therefore, a cilia deformation results in a variation of the magnetic field at the sensor surface and therefore in a measurable electrical signal that can be correlated with textural features.

A. Magnetic cilia

The magnetic elastic composite is achieved by mixing NdFeB particles, with an average diameter of 5 μm with a PDMS[1] quasi-elastic polymeric matrix. This composite was optimized to achieve the maximum possible magnetic particle concentration (which is linearly proportional to the magnetic field amplitude of the cilia) while still maintaining an elastic characteristic (as a high concentration of magnetic particles makes the composite brittle). Furthermore, the pillars were fabricated in a completely separate process from the TMR sensors, being later assembled on top of the sensors using plasma bonding [18]. A schematic view of the cilia production process is presented in Fig. 2.

[1]PDMS was prepared from Sylgard 184 at a mass proportion of 15 parts of elastomer to 1 part of curing agent

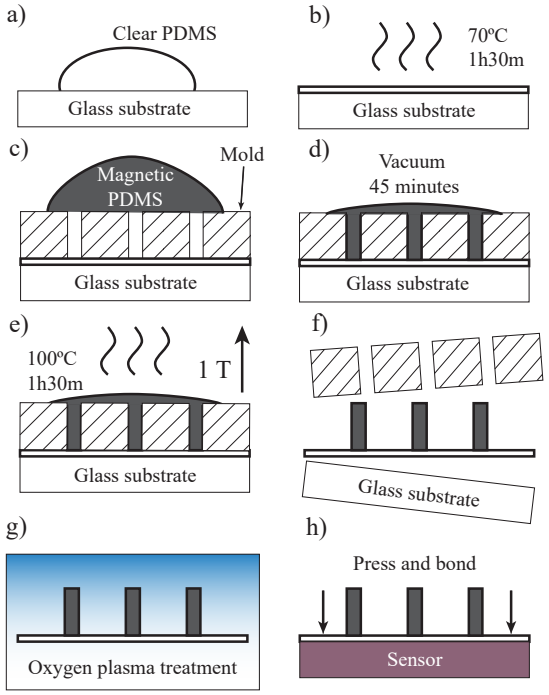

Fig. 2. Fabrication steps of the magnetic cilia.

The fabrication of the pillars starts by producing a thin layer of 200 μm of simple PDMS by spin-coating on top of a dummy glass substrate and left to cure for 1 hour and 30 minutes in an oven set at 70° C (Fig. 2 a) and b)). The usage of a 200 μm layer of PDMS ensures that the layer (and everything fabricated on top of it) is easily peelable from the glass substrate. It is of critical importance that clear PDMS is used for this layer, as the presence of magnetic particles can contaminate the magnetic signal to be measured by the sensor.

When this thin-layer is cured, a laser drilled Poly(methyl methacrylate) (PMMA) mold with the desired pillar width and height is placed on top of the PDMS thin-layer and clamped to the substrate.

A mix of PDMS with a 65% mass proportion of NdFeB particles was poured over the mold (Fig. 2 c)) and placed inside a vacuum chamber for 45 minutes, for the PDMS to fill in the voids within the mold (Fig. 2 d)). Finally, the sample was placed in a 100° C oven for 1 hour and 30 minutes to cure the PDMS with magnetic particles (Fig. 2 e)), while a 1 T magnetic field was applied in the pillars axial direction, in order to set their magnetization.

A 149 kA/m magnetization was measured on the finished composite. Given that the total cilia volume on a sensor will range from 1.44 mm^3 to 1.8 mm^3 per cilium, the magnetic moment of the cilia will never be greater than 268 μAm^2, resulting in an estimated (ideal) maximum magnetic field incident on the sensor of 3 mT, which is below the saturation magnetic field of the used magnetic sensor.

After curing is complete, the mold is removed and the PDMS structures are peeled off the glass substrate (Fig. 2 f)). Transfering is done to the previously fabricated sensor by plasma bonding, where both the PDMS pillars and the sample were exposed to an oxygen plasma (Fig. 2 g)) and pressed against each other immediately afterwards, ensuring a permanent bonding (Fig. 2 h)). Once cilia-sensor bonding is complete, the sensor is wirebonded to a miniature PCB with a dimension of 6 x 6 mm^2 and equipped with a 6 contact miniature connector, to be connected to the data acquisition and conversion board.

B. TMR sensor

The sensor was microfabricated at INESC-MN, with the x and y detection orientations integrated within the same wafer, both arranged in a Wheatstone bridge configuration, as it provides an easier signal conditioning and improved noise characteristics [19]. The process used to fabricate these sensors is a variant of the one used to produce hard-drive disk heads, enabling mass-production at wafer scale of these sensors.

The Wheatstone bridge configuration is frequently used for magnetoresistive sensor systems, with the additional advantage that many electronic architectures exist to compensate for its non-idealities. [20] [21].

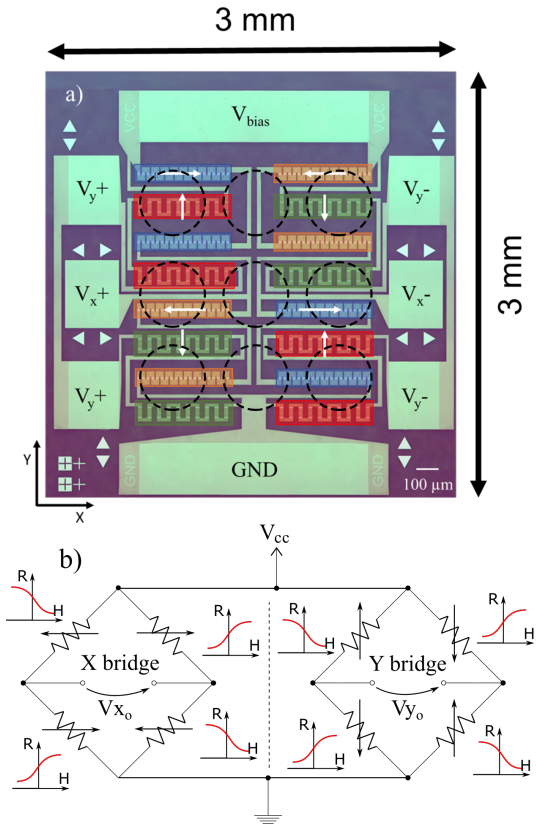

Fig. 3. a) Microphotograph of the produced TMR sensor. The white arrows indicate the sensitive direction of each sensor region. Regions of the same colour have the same sensitive direction. The dashed circles show the cilia position on top of the sensor. b) Schematic of the fabricated die, with the expected response of each TMR element.

The Wheatstone bridge schematic is presented in Fig. 3 and the differential voltage across its branches is given by (see Fig. 4 for nomenclature)

$$\mathrm{V_o} = \left(\frac{R_2}{R_1 + R_2} - \frac{R_4}{R_3 + R_4} \right) \mathrm{V_{cc}}, \tag{1}$$

which, assuming the resistance of each sensor is given by linear equation $R_i = A_i H$ (which is a good approximation around H = 0), results in $A_1 = A_2 = A_3 = A_4 \Rightarrow V_o = 0$ for this ideal case. Thus, in order to observe the linear response in the bridge, it is necessary that $A_1 = A_3 = -A_2 = -A_4$, i.e. elements $R_{1,3}$ and $R_{2,4}$ must have anti-parallel sensitivities.

Therefore, 4 sensitive elements are required for this device, since it employs 2D sensitivity and each of sensitive direction requires two anti-parallel sensitive elements for the bridge to be assembled.

In order to achieve this, a top-pinned amorphous alumina barrier magnetoresistive stack was chosen, (with the structure, from bottom to top: [Ta 5/Ru 15]x3/$Ni_{80}Fe_{20}$ 4/Al_2O_3 1.4/$(Co_{80}Fe_{20})_{90}B_{10}$ 3/Ru 0.6/$Ni_{80}Fe_{20}$ 3/$Mn_{75}Ir_{25}$ 18/Ru 5/Ta 5, thicknesses in nm). This type of structure is easy to produce and straighforward to integrate with other sensitive directions within the same substrate, with the disadvantage of not being resilient to high temperatures (with the possibility of permanently impacting performance for temperatures above 100° C) [22][23].

The TMR stack was patterned into sensing elements of 2x20 μm area, and connected in series with other elements with the same sensitive direction to form each sensing array with 80 sensing elements in series (Fig. 3). All the interconnections between the elements and to other sensitive elements forming the Wheatstone bridge were fabricated by lithography patterning and deposition of a 300 nm AlSiCu metallization layer. Finally, the device was passivated with 200 nm Al_2O_3/200 nm SiO_2, not only to protect the active elements of the device, but also to promote the adhesion of the magnetic cilia to the device in the final stage of the sensor fabrication process.

The produced devices demonstrated an average equivalent resistance of 14 kΩ, and is powered by a biasing voltage of $\mathrm{V_{bias}} = 1.25$ V, which results in a sensor power consumption of 112 μW. The fabricated device has a sensitivity of 6.38 mV/mT within a linear range of $\pm$5 mT.

C. Analog front-end

The analog front-end conditions the output signal from both Wheatstone bridges (X and Y directions), performing offset trimming and filtering as well as amplification and analog to digital conversion of the signal. The assembled device (with the sensor mounted on this analog-front end) uses a supply voltage of 3.3 V, consuming 4.9 mW of power when actively measuring the sensor and achieving a micropower consumption of 13 μW when in standby mode. The circuit schematic is presented in Fig. 4.

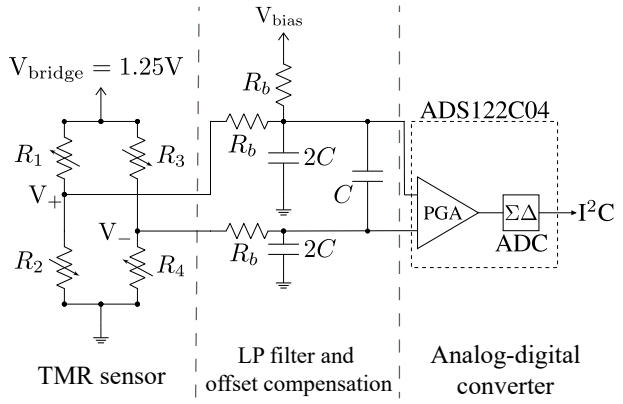

Fig. 4. Schematic of the electronic front-end with offset compensation.

1) Offset trimming: Although in the ideal case R_{1-4} is the same when $H = 0$ and the bridge is always balanced [2], with real devices a mismatch between sensors resistance at zero magnetic field always exist, thus unbalancing the bridge and leading to the existence of an offset on the Wheatstone bridge response.

This offset is highly undesirable as it limits the amplification that can be applied to the signal, and therefore an architecture to analogically compensate this offset before the amplification step was implemented.

The amplifier bias nulling architecture [21] was chosen, in which the positive bridge branch is unbalanced by applying a voltage bias to it through a resistance $R_b \gg R_{1-4}$, making the response of the sensor take the form (at the ADC input)

$$V_o \approx \left(\frac{R_2}{2(R_1 + R_2)} - \frac{R_4}{R_3 + R_4} \right) + \frac{1}{2} V_{bias}, \qquad (2)$$

which allows trimming of the offset by controlling the V_{bias} voltage, but with the disadvantage of reducing the sensitivity[3] to 75% of the observed if the compensation method was not implemented.

2) Filtering: Although all the experiments were performed at a 40 SPS data rate, the device is still susceptible to noise arising from aliasing without adequate filtering at the ADC input. To prevent this, a 230 Hz first-order fully differential low pass filter was implement for the device by setting $R_b = 100$ kΩ and $C = 3400$ pF to mitigate the noise caused by aliasing.

3) Analog to digital converter: The trimmed and filtered analog signal is sent to a Texas Instruments ADS122C04 fully-differential analog-to-digital converter (ADC) unit. This unit is equipped with an integrated programmable gain amplifier input stage and 50 Hz notch filter, which further conditions the signal before reaching the ΣΔ conversion unit where the signal is converted into a 24-bit digital word. This unit communicates the result of the conversion through an I^2C bus, with a 40 SPS data rate being used for testing (although data rates up to 2 kSPS are possible). The dynamic response of the device is expected to be limited to 230 Hz vibrations, although this figure may be lower due to the dynamic mechanical behaviour of the cilia, which was not evaluated for this work.

[2]A magnetoresistive Wheatstone bridge is balanced when $V_o(H = 0) = 0$

[3]Sensitivity S is defined as the voltage rate of change with applied magnetic field $S = \frac{dV_o}{dH}$

III. Experimental method

Two types of textured media were evaluated using this device:

- **Repeatability**: The device was actuated 10 times to test its stability to repeated actuations.
- **Unpatterned textures**: Textures with known surface roughness, but with a random and isotropic feature distribution.
- **Patterned textures**: Texture with features of which the width, height and position within the sample is known.

A. Repeatability

In order to test the stability of the cilia sensor system, a test was performed where the cilia would be made to move under a flat indentor at a height of 1 mm from the sensor surface, following the cycle (Fig. 5):

1) Right cilia gets in contact with indentor
2) All cilia are bent under the indentor
3) Cilia release contact with the indentor
4) Left cilia gets in contact with indentor
5) All cilia are bent under the indentor
6) Cilia release contact with indentor

The indentor was kept at a distance of 1 mm from the sensor surface, and values were measured for fixed positions under the indentor.

B. Unpatterned textures

A selection of sandpaper with various grits was used, as the surface roughness of these tools is regulated by the ISO 6344 international standard. The used types of sandpaper used and their respective surface roughnesses as presented in table I [24] [25].

TABLE I
Relation between sandpaper grit and surface roughness

Sandpaper grit	Surface roughness (μm)
40	212.5
120	59.5
240	30.0
320	23.1
500	15.1
1000	9.2

To measure the surface roughness, the various types of sandpaper were fixed to a PMMA support, which was fixed at a constant distance of 1 mm from the sensor surface (independently of the cilia height, diameter or disposition). The sensor itself was attached to a Cartesian motorized stage and made to move at a constant velocity of 1 mm/s as the cilia brushed against the sandpaper (Fig. 6 a)). Since the tested texture media are unstructured, the surface roughness was correlated with the standard deviation of the signal measured while it brushed each type of sandpaper.

C. Patterned textures

For patterned textures, a series of structures were fabricated using SU-8 (photosensitive polymer) with various thicknesses over a silicon substrate.

The process used to measure the height and width of the patterned structures was the same as described in the previous subsection (but with the scanning speed reduced to 0.5 mm/s to achieve higher spatial resolution), and the height of the patterned structure was correlated with the amplitude of measured signal step (Fig. 6 b)).

IV. Results

All results are presented in terms of the ADC measured number of least-significant bits (LSB). Three cilia configurations were tested:

- **Configuration A**: Three pillars in line, each with 360 μm diameter and 3 mm height.
- **Configuration B**: Nine pillars as a 3x3 array over the sensor, each with 400 μm diameter and 3 mm height.
- **Configuration C**: Nine pillars as a 3x3 array over the sensor, each with 360 μm diameter and 1.6 mm height.

The heights and diameters chosen for the cilia are limited by the production capabilities of the used CO_2 laser cutting equipment.

A. Response to consecutive actuations

The cycle of cilia actuation was repeated 10 times without any noticeable drift, as can be seen in Fig. 5. The maximum measured dispersion was of 0.05 (5%), with this figure being calculated as the range of measured values for each position, divided by the minimum measured value, thus confirming the reliability of the tested device. It should also be noticed that an assymetry was measured between the forward and back motion, which is mostly likely due to a misalignment of the cilia on top of the sensor (as these were placed manually).

B. Unpatterned surface measurement

The measured sensor data while the cilia contacted with a specific sandpaper type was divided into intervals of 20 points, with the standard deviation being computed for each interval. As texture measurement will manifest itself as a high frequency characteristic, and in order to exclude continuous influences from the signal (such as the Earth's magnetic field), the linear component of the signal was removed (by subtracting the best fitting linear regression from each interval) before computing the standard deviation.

2500 measurements of the sensor signal were made as it was actuated by the various types of sandpaper, resulting in 125 measured standard deviation values for each surface roughness. These standard deviation values were fitted to a Gaussian distribution, and the average values and 95% confidence intervals are presented in figure 7.

Cilia configurations where the height of the pillar is larger (configurations A and B) result in a larger signal than when the same sample is measured with the smaller cilia. At a 95% confidence interval, it is noted that for all cilia configurations it is not possible to distinguish between higher surface roughnesses, as the uncertainty of the measurement tends to increase with the sandpaper surface roughness. However, for lower surface roughness, for configurations A and B, small values of surface roughness (between 9 μm and 30 μm) are distinguishable.

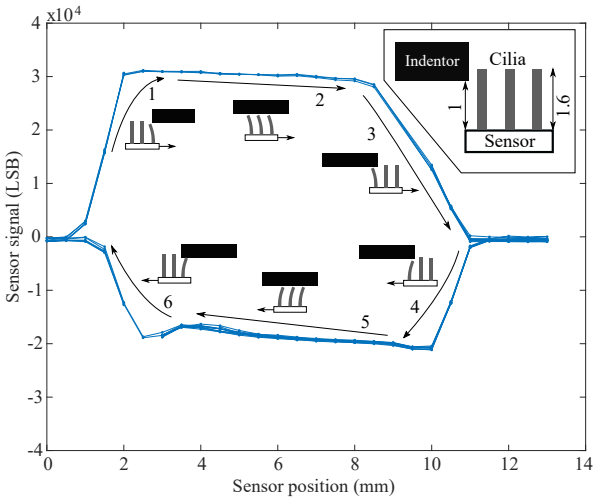

Fig. 5. Repeatability test results. The sensor was made to move through an indentor, repeating this cycle 10 times. **Inset**: Dimensions of the cilia used in this test.

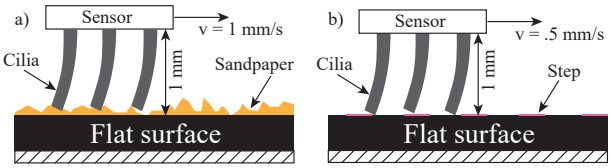

Fig. 6. Diagram of the performed topography scanning experiments using the cilia sensor for unpatterned (a) and patterned structures (b)

This is expected, as the larger length of the pillars will promote a greater deflection. This combined with the difference in magnetic pillar volume (configurations B and C have 3 times more cilia volume than configuration A) results in a stronger signal, leading to a larger signal to noise ratio.

C. Patterned surface measurement

For patterned textures, configurations A and B were tested. The patterned structures were fabricated as strips with approximately 200 μm width, and heights of 20 μm and 50 μm. For configuration A, with the measured data during the actuation presented in Fig. 8 b), both the 20 μm step and the 50 μm step present a noticeable variation on the signal, with a higher difference in measured signal appearing when the sensor is actuated by a higher step. The 20 μm step resulted in a measured signal of 573 bits, while the 50 μm step resulted in an average measured signal of 2259 bits.

For configuration B however, with the measured signal during the actuation presented in Fig. 8 c), only the 50 μm step presents a change in signal, while the smaller 20 μm step does not present a change in signal that is distinguishable from the noise background. The 50 μm step resulted in an average measured signal of 1236 bits (although with low

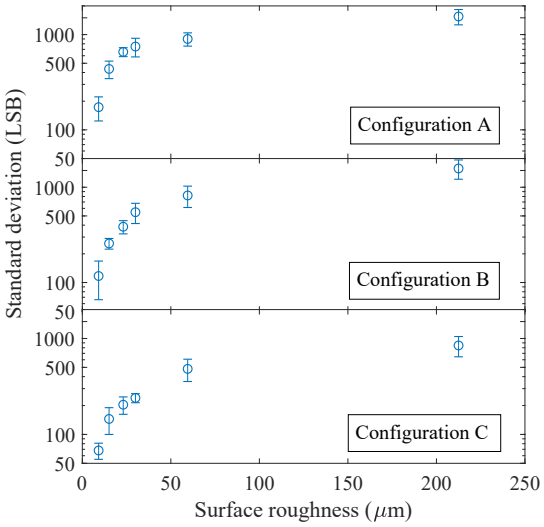

Fig. 7. Standard deviation of the measured signal for each sandpaper surface roughness. The error bar represents the 95% confidence interval of each measurement.

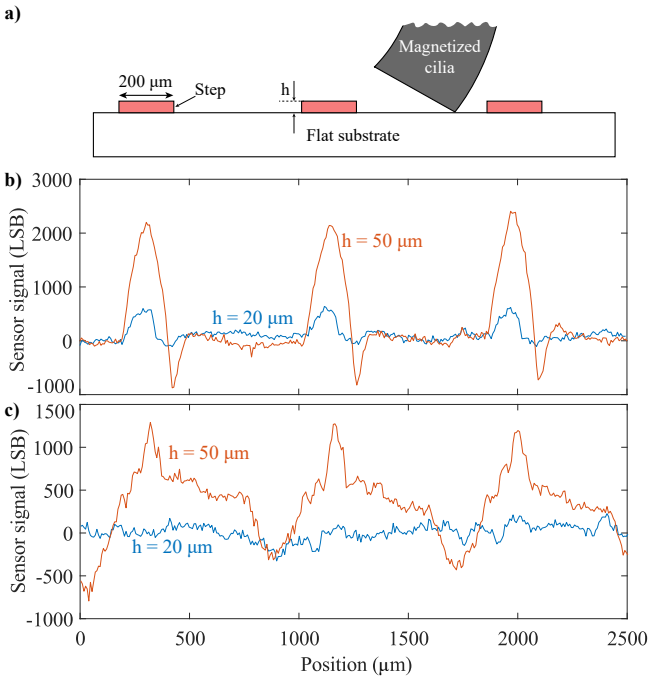

Fig. 8. a) Representation at scale of the cilia crossing the patterned steps b) Measured signal for a sensor with configuration A cilia when actuated by the patterned 20 μm (blue line) and 50 μm (orange line) structures. c) Measured signal for a sensor with configuration B cilia when actuated by the patterned 20 μm (blue line) and 50 μm (orange line) structures.

spatial resolution).

It is of interest to note that there is broadening of the measured signal step when the cilia configuration changes from 3 actuating cilia in line to 9 actuating cilia in a 3x3 matrix, confirming that when the cilia area of contact decreases this leads to a higher spatial resolution and the ability of detecting finer textural features.

V. Conclusion

This paper focused on the design and fabrication of a texture topography sensor, and proposes an electronic front-end architecture to modularize the device with offset correction and on-board analog-to-digital conversion.

For the case of unpatterned structures, the sensor was observed to be able to distinguish between surfaces roughness of 9 μm to 15 μm, but unable to achieve this for higher surface roughnesses, as an increase on the uncertainty of the surface roughness measurement occurs when more coarse textures are tested. This represents an improvement in resolution when compared with the previously developed cilia sensor in [15], and despite presenting a much smaller footprint than the device reported by [8], far from its reported resolution of 400 nm. The best performing cilia configuration, for the cases where spatially resolving the surface topography under test is not required, was the 3x3 arrangement with 3 mm high cilia, most likely due to the larger volume of magnetic material present on this configuration when compared with the remaining ones.

For patterned structures, a sample with a series of 20 μm and 50 μm high steps was tested. In this case, the best performing sensor corresponded to the one where the 3mm high cilia were disposed in a 3 cilia line, which was capable of resolving both steps. To the best of our knowledge, this is the lowest reported thickness feature scanned with a tactile sensor. This configuration has the lowest area of contact leading to the highest spatial resolution. The configuration with 3x3 cilia cannot detect the 20 μm step, and presents a broader signal when the cilia crosses the step, which is consistent with a loss of spatial resolution due to it having a larger actuating area.

For future work, the exploration and classification of patterned textures (like skin or textiles) will be studied, and the usage of the 2D sensitivity of the TMR magnetic sensor (which was not used in this study) will be tested in order to determine how to best take advantage of this feature for both texture and force measurements.

Acknowledgements

We thank FabLab Lisboa for providing access and assistance with the laser cutting equipment. P. Ribeiro acknowledges FCT for his PhD grant SFRH/BD/130384/2017. S. Cardoso acknowledges FCT for grants NORTE-01-0145-FEDER-22090, MAGLINE-LISBOA-01-0247-FEDER-17865 and MagScopy4IHC-LISBOA-01-0145-FEDER-031200. A. Bernardino acknowledges FCT project UID/EEA/50009/2019 and European Commission project ORIENT (ERC/2016/693400). This work was partially supported by the EPSRC UK (with projects MAN3, EP/S00453X/1, and NCNR, EP/R02572X/1).

References

[1] M. Bjorkman, Y. Bekiroglu, V. Hogman, and D. Kragic, "Enhancing visual perception of shape through tactile glances," in *2013 IEEE/RSJ International Conference on Intelligent Robots and Systems*, IEEE, nov 2013.

[2] R. S. Dahiya, P. Mittendorfer, M. Valle, G. Cheng, and V. J. Lumelsky, "Directions toward effective utilization of tactile skin: A review," *IEEE Sensors Journal*, vol. 13, pp. 4121–4138, nov 2013.

[3] R. Dahiya, G. Metta, M. Valle, and G. Sandini, "Tactile sensing—from humans to humanoids," *IEEE Transactions on Robotics*, vol. 26, pp. 1–20, feb 2010.

[4] W. Yuan, S. Dong, and E. Adelson, "GelSight: High-resolution robot tactile sensors for estimating geometry and force," *Sensors*, vol. 17, p. 2762, nov 2017.

[5] H. Yamazaki, M. Nishiyama, K. Watanabe, and M. Sokolov, "Tactile sensing for object identification based on hetero-core fiber optics," *Sensors and Actuators A: Physical*, vol. 247, pp. 98–104, aug 2016.

[6] D. Hughes and N. Correll, "Texture recognition and localization in amorphous robotic skin," *Bioinspiration & Biomimetics*, vol. 10, p. 055002, sep 2015.

[7] W. Liu, P. Yu, C. Gu, X. Cheng, and X. Fu, "Fingertip piezoelectric tactile sensor array for roughness encoding under varying scanning velocity," *IEEE Sensors Journal*, vol. 17, pp. 6867–6879, nov 2017.

[8] Z. Yi, Y. Zhang, and J. Peters, "Bioinspired tactile sensor for surface roughness discrimination," *Sensors and Actuators A: Physical*, vol. 255, pp. 46–53, mar 2017.

[9] T. A. Keil, "Functional morphology of insect mechanoreceptors," *Microscopy Research and Technique*, vol. 39, pp. 506–531, dec 1997.

[10] F. Li, W. Liu, C. Stefanini, X. Fu, and P. Dario, "A novel bioinspired PVDF micro/nano hair receptor for a robot sensing system," *Sensors*, vol. 10, pp. 994–1011, jan 2010.

[11] Y. Tang, R. L. Peterson, and K. Najafi, "Technology for fabricating dense 3-d microstructure arrays for biomimetic hair-like sensors," in *2013 IEEE 26th International Conference on Micro Electro Mechanical Systems (MEMS)*, IEEE, jan 2013.

[12] A. Virta, J. V. Timonen, R. H. Ras, and Q. Zhou, "Force sensing using artificial magnetic cilia," in *2012 IEEE/RSJ International Conference on Intelligent Robots and Systems*, IEEE, oct 2012.

[13] A. Alfadhel, B. Li, A. Zaher, O. Yassine, and J. Kosel, "A magnetic nanocomposite for biomimetic flow sensing," *Lab Chip*, vol. 14, no. 22, pp. 4362–4369, 2014.

[14] A. Alfadhel and J. Kosel, "Magnetic nanocomposite cilia tactile sensor," *Advanced Materials*, vol. 27, pp. 7888–7892, oct 2015.

[15] P. Ribeiro, M. A. Khan, A. Alfadhel, J. Kosel, F. Franco, S. Cardoso, A. Bernardino, A. Schmitz, J. Santos-Victor, and L. Jamone, "Bioinspired ciliary force sensor for robotic platforms," *IEEE Robotics and Automation Letters*, vol. 2, pp. 971–976, apr 2017.

[16] A. Alfadhel, M. A. Khan, S. C. de Freitas, and J. Kosel, "Magnetic tactile sensor for braille reading," *IEEE Sensors Journal*, vol. 16, pp. 8700–8705, dec 2016.

[17] P. Ribeiro, M. A. Khan, A. Alfadhel, J. Kosel, F. Franco, S. Cardoso, A. Bernardino, J. Santos-Victor, and L. Jamone, "A miniaturized force sensor based on hair-like flexible magnetized cylinders deposited over a giant magnetoresistive sensor," *IEEE Transactions on Magnetics*, vol. 53, pp. 1–5, nov 2017.

[18] S. Bhattacharya, A. Datta, J. Berg, and S. Gangopadhyay, "Studies on surface wettability of poly(dimethyl) siloxane (PDMS) and glass under oxygen-plasma treatment and correlation with bond strength," *Journal of Microelectromechanical Systems*, vol. 14, pp. 590–597, jun 2005.

[19] P. P. Freitas, S. Cardoso, R. Ferreira, V. C. Martins, A. Guedes, F. A. Cardoso, J. Loureiro, R. Macedo, R. C. Chaves, and J. Amaral, "Optimization and integration of magnetoresistive sensors," *SPIN*, vol. 01, pp. 71–91, jun 2011.

[20] J. S. Moreno, D. R. Muñoz, S. Cardoso, S. C. Berga, A. E. N. Antón, and P. J. P. de Freitas, "A non-invasive thermal drift compensation technique applied to a spin-valve magnetoresistive current sensor," *Sensors*, vol. 11, pp. 2447–2458, feb 2011.

[21] Honeywell International Inc., "Handling sensor bridge offset." Application Note 212.

[22] S. Cardoso, V. Gehanno, R. Ferreira, and P. Freitas, "Ion beam deposition and oxidation of spin-dependent tunnel junctions," *IEEE Transactions on Magnetics*, vol. 35, no. 5, pp. 2952–2954, 1999.

[23] S. Knudde, D. C. Leitao, S. Cardoso, and P. P. Freitas, "Annealing free magnetic tunnel junction sensors," *Journal of Physics D: Applied Physics*, vol. 50, p. 165001, mar 2017.

[24] International Organization for Standardization, "ISO 6344-2:1998: Coated abrasives — Grain size analysis — Part 2: Determination of grain size distribution of macrogrits P12 to P220," 1998.

[25] International Organization for Standardization, "ISO 6344-3:2013: Coated abrasives — Grain size analysis — Part 3: Determination of grain size distribution of microgrits P240 to P2500," 2013.